This is the author's version of an article that has been published in this journal. Changes were made to this version by the publisher prior to publication.
The final version of record is available at http://dx.doi.org/10.1109/JSEN.2020.2971595

Characterization of a Miniaturized IR Depth Sensor with a Programmable Region-of-Interest that Enables Hazard Mapping Applications

Ryan M. Jans, Adam S. Green, Lucas J. Koerner, *Member, IEEE*

***Abstract*—Ultrasonic sensors have dominated miniaturized depth measurement applications such as robot collision avoidance and walking cane hazard detection yet have limited spatial resolution. Optical time-of-flight (ToF) depth sensors offer the potential for improved spatial resolution, however, ToF depth-sensing cameras may be too large and power-hungry for hand-held applications. We address this gap by experimentally evaluating an infrared ToF sensor (the ST VL53L1X) that uses a single-photon avalanche photodiode array to provide coarse spatial resolution while remaining miniaturized and low-power, thus allowing the generation of hazard maps in hand-held applications. We develop methods and present characterization results for distance measurement accuracy, noise, error, and tolerable ambient illumination. The IR ToF sensor sustains accuracy better than 2% up to a distance of 3000 mm for a 73% reflective target in the presence of zero interfering ambient light. We characterize the spatial resolution enabled by this region-of-interest and find off-axis pointing of up to 15.7° in steps of 2.5°. Many hazard detection systems may be moving, which dynamically changes the position and pointing of the depth sensor. We demonstrate the use of a 9-degree-of-freedom (3-axis accelerometer, gyroscope, and magnetometer) inertial measurement unit (IMU) to track sensor pointing. The ToF sensor combined with an IMU forms the basis for a miniaturized depth mapping solution that consumes 97.5 mW when operating at 30 Hz, and requires simple serial interfaces to a microcontroller.**

***Index Terms*—**

I. Introduction

DEPTH sensing is a critical technology for hazard detection used in autonomous robots [1] or smart canes that assist visually challenged individuals [2], [3]. Ultrasonic depth sensors that measure the time-of-flight (ToF) of an acoustic echo have been commonly used [4]–[6] but are physically large and not robust to environmental parameters such as humidity and air pressure [7]–[9]. Recently, the capabilities of miniaturized optical ToF sensors have improved due to developments in single-photon avalanche photodiodes (SPADs), time-to-digital converters (TDCs), and power-efficient vertical-cavity surface-emitting lasers (VCSELs) [10]. IR ToF sensors offer compelling advantages over ultrasonic sensors including improved angular resolution with the possibility of programmable region-of-interest (ROI) to adjust pointing, a smaller physical form-factor, and faster frame rates.

A. Green is with the Department of Physics, University of St. Thomas, St. Paul MN, 55105, USA

L. Koerner and R. Jans are with the Department of Electrical and Computer Engineering, University of St. Thomas, St. Paul MN, 55105, USA e-mail: (koerner.lucas@stthomas.edu).

This work evaluates depth sensing solutions for applications that are mobile yet slow-moving and require a low-power miniaturized sensor system. Hazard detection for the white cane of a visually impaired user is a specific application we target in this work [2], [3], [11]. Such an application anticipates a typical walking speed of $\sim 1.4\,\mathrm{m/s}$. To issue a warning at least $1\,\mathrm{s}$ before a collision the sensor must accurately measure depths at a target distance of $1.4\,\mathrm{m}$. In addition, for a battery run-time of $24\,\mathrm{hrs}$, a system powered by a rechargeable AA or equivalent battery (e.g. the Duracell DX1500 with a $10\,800\,\mathrm{J}$ energy capacity [12]) must consume $125\,\mathrm{mW}$ or less. These specifications, plus a modest spatial resolution to discern the location of hazards, direct the depth-sensing solution in this study.

Depth sensing cameras, which use fast photodiodes to measure the phase shift added by travel time to sinusoidally modulated illumination [13]–[15], are commercially available. An example of such a ToF sensor is the Sony IMX556, a 680×480 sensor array with $10\,\mu\mathrm{m}$ pixels and an $8\,\mathrm{mm}$ sensor diagonal that detects emitter modulation up to $100\,\mathrm{MHz}$. The IMX556 has been built into cameras including the *Helios Embedded* from LUCID Vision Labs with a power consumption $<15\,\mathrm{W}$, a long working range of up to $6\,\mathrm{m}$, and an error $<5\,\mathrm{mm}$ from $0.3\,\mathrm{m}$ to $1.5\,\mathrm{m}$ [16]. Other commercial sensors include a a 224×172 array from Infineon (IRS1645C) [17]. Pmdtechnologies has incorporated the IRS1645C into a camera (*pico flex*), with a depth resolution better than $2\,\%$ up to $1\,\mathrm{m}$ and a power consumption of $300\,\mathrm{mW}$ (at $45\,\mathrm{fps}$) [18]. These camera developments point to where ToF is headed and demonstrate the rapid pace of innovation, yet may not be appropriate for certain hand-held applications due to high power consumption, large size, and a need for down-stream image processing.

Single-pixel and small array depth sensors have been built from SPADs which enable direct ToF, an architecture that measures the time-of-flight of individual photons [19], [20]. A direct ToF signal chain utilizes an avalanche photodiode, a time-to-digital converter, digital logic, and memory to construct a histogram of photon flight times [21]–[23]. Large format SPAD arrays are technologically challenging, so direct ToF solutions are typically limited in spatial resolution, but provide miniaturized, low-power alternatives to ToF imaging cameras. Examples include the Broadcom AFBR-S50MV85G 16 SPAD array [24] and the ST VL53L0X SPAD array [25], [26]. A third example is the ST VL53L1X which uses a 16×16 silicon SPAD array with a $940\,\mathrm{nm}$ VCSEL emitter that allows

Copyright (c) 2020 IEEE. Personal use is permitted. For any other purposes, permission must be obtained from the IEEE by emailing pubs-permissions@ieee.org.

This is the author's version of an article that has been published in this journal. Changes were made to this version by the publisher prior to publication.
The final version of record is available at http://dx.doi.org/10.1109/JSEN.2020.2971595

for depth measurements up to $4\,\mathrm{m}$ with a full field-of-view of $27°$ and a power consumption of $20\,\mathrm{mW}$ at a frame-rate of $10\,\mathrm{Hz}$ [27]. The enabled SPADs are programmable so that the field-of-view can be adjusted in size and shifted off-axis [27]. Here we demonstrate how the ST VL53L1X fills a gap between single point depth sensors and high power depth-sensing cameras by being low-power and miniaturized while also providing coarse spatial resolution.

In this work, we characterize the depth measurement accuracy of the ST VL53L1X optical and the HC-SR04 ultrasonic ToF sensors versus target reflectivity and sensor mode. The HC-SR04 is intended as a commonly available reference for comparison; state-of-the-art ultrasonic depth sensors show performance gains over the HC-SR04 driven by novel signal processing methods [28], [29]. Performance characteristics unique to the VL53L1X are then presented. A noteworthy feature of the VL53L1X is the programmable ROI. An important contribution of this work is our demonstration and characterization of the spatial resolution enabled by the programmable ROI. Furthermore, optical ToF sensors are typically hindered by an inability to detect objects of low optical reflectivity. We leveraged the programmable ROI feature to detect an object of low reflectivity surrounded by one of high reflectivity. Our measurements demonstrate that the VL53L1X, when coupled to an inertial measurement unit (IMU), creates a system for low-power hazard mapping. A significant limitation of direct optical ToF sensors is performance degradation in the presence of ambient illumination. We demonstrate an experimental methodology to characterize the noise of the depth measurement versus the intensity of ambient illumination and show that the noise of the distance measurement is determined by the ratio of the signal rate to the ambient rate. Characterization data is archived and publicly available [30].

II. Methods

A. Sensor System

An STM32 microcontroller development board (NUCLEO-F411RE) interfaced with the sensors and a host computer. The microcontroller, configured over a serial connection with the host computer, ran desired tests, set sensor parameters and acquired sensor data over I2C, and transferred results to the host computer. The microcontroller system clock was set to $72\,\mathrm{MHz}$ for prompt transfer to the host computer (115200 baud) and high-resolution time-to-digital conversion of the ultrasonic sensor output pulse.

Fig. 1 shows the ST VL53L1X ToF sensor mounted on an expansion board (X-NUCLEO-53L1A1) that interfaces with the Nucleo-F411RE via stacking headers. The VL53L1X ToF sensor uses a $940\,\mathrm{nm}$ Class 1 laser emitter and a 16x16 SPAD array to collect ranging data. The FoV is programmable from $15°$ to $27°$. Additional data includes return signal rate, ambient rate, a measurement counter, range status, and the number of enabled SPADs. These data were transferred to the host computer and written to an output file.

The HC-SR04 sensor (Adafruit 3942) is an accessible, low cost ranging ToF sensor. The FoV is fixed at $15°$. The ultrasonic modulation frequency is $40\,\mathrm{kHz}$; measurements are triggered by a $10\,\mu\mathrm{s}$ high input signal pulse. This sensor is independent of target optical reflectivity but sensitive to the target material, as well as temperature and humidity of the air due to changes in the speed of sound. The microcontroller counts the time that the HC-SR04 output is asserted high using the $72\,\mathrm{MHz}$ system clock for the final depth result.

Environmental data was recorded by a Silicon Labs Thunderboard Sense 2 (SLTB004A). This sensor gathers environmental data using the Si7021 temperature and humidity sensor; as well as UV intensity and ambient light illuminance (lux) using the Si1133. The spectrum of the ambient illumination was characterized by a hand-held spectrometer (Ocean Optics, FLAME-S-VIS-NIR-ES). Ranging accuracy was verified using a Fluke 414D laser distance meter accurate to $\pm 3\,\mathrm{mm}$ and mechanically coupled to the sensor apparatus. The apparatus, which contained the microcontroller, VL53L1X ToF sensor, ultrasonic sensor, and rangefinder, was fixed to an optical breadboard mounted to a camera tripod. The microcontroller with the VL53L1X ToF sensor and ultrasonic sensor were mounted in the same plane with an offset height of $50\,\mathrm{mm}$. To properly fill the FoV in relation to the background, the sensor center height was set to $1.524\,\mathrm{m}$.

B. ToF Sensor Configuration Modes

The VL53L1X ToF sensor characteristics were evaluated, using various ranging modes and timing budgets. Three distance modes (DM) are available: short, medium, and long. The minimum ranging distance for all modes is $4\,\mathrm{cm}$, however, the maximum ranging distance varies with mode. Short DM provides better ambient immunity with a $1.3\,\mathrm{m}$ maximum distance. Medium ranging provides a $3\,\mathrm{m}$ range, while long ranging provides a maximum range of $4\,\mathrm{m}$ but is more sensitive to ambient illumination. The timing budget (TB) sets and is bound from $20\,\mathrm{ms}$ to $1000\,\mathrm{ms}$. The minimum inter-measurement period must be longer than the timing budget plus $4\,\mathrm{ms}$ otherwise an error is returned.

C. Target Setup

The left photograph of Fig. 1 shows the setup of a near target suspended in front of a background that fills the full FoV of the sensor. The three main backgrounds were $0.5\,\mathrm{in}$ rigid foam core with respective reflectivities of 8%, 23%, and 73%. The background spanned $2\,\mathrm{m}$ by $2\,\mathrm{m}$ and was set perpendicular to the floor. Near targets consisted of $13\,\mathrm{cm}$ by $13.5\,\mathrm{cm}$ cardboard painted with the desired reflectivities. These targets were suspended from an overhead wire and fixed at a certain distance from the background in tests. Similarly to the background setup, targets were aligned with the center of the sensor apparatus and perpendicular to the floor.

D. Reflectivity Testing

The reflectivity of targets can have a major impact on IR ToF sensors due to possible losses in signal return rate from a target. Testing of all three background/target reflectivities was conducted using a white light source, a backscatter reflection probe, and a spectrometer. Calibration was performed

Copyright (c) 2020 IEEE. Personal use is permitted. For any other purposes, permission must be obtained from the IEEE by emailing pubs-permissions@ieee.org.

This is the author's version of an article that has been published in this journal. Changes were made to this version by the publisher prior to publication.
The final version of record is available at http://dx.doi.org/10.1109/JSEN.2020.2971595

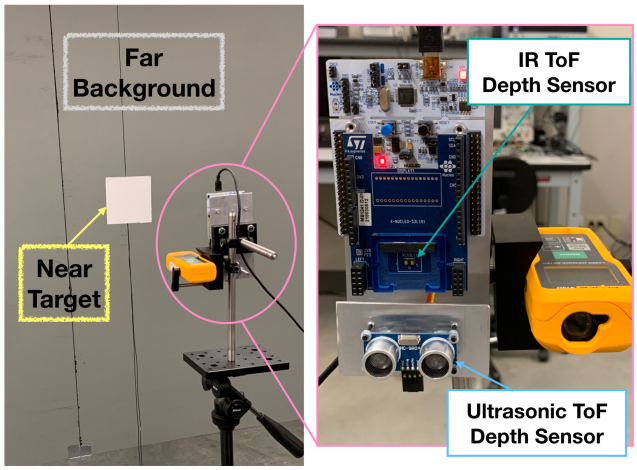

Fig. 1. Labeled photographs of the experimental setup which show the suspended near target and far background (left) and the sensor system (right). The sensor system includes the IR ToF, Ultrasonic ToF, reference laser range finder, and the master microcontroller board.

using diffuse reflectance standards (Labsphere, USRS-99-010 and Ocean Optics WS-1, STAN-SSH). Upon calibration, two combinations of light incidence and reflection angles were measured: normal incidence and normal reflection, which is reported as the reflectivity, and normal incidence with $45°$ reflection, to verify the assumption that the targets are Lambertian scatterers. Spectral data ranged from $350\,\mathrm{nm}$ to $1000\,\mathrm{nm}$ for each of the three targets. The reflectivity reported is the value measured at $940\,\mathrm{nm}$, which is the center wavelength of the ToF sensor IR emitter [27].

III. Experimental Characterization

A. Noise and accuracy

Fig. 2 shows the measured distance, non-linearity, and noise of the IR ToF and the ultrasonic distance measurement sensors. At each distance, 500 measurements are captured from the ultrasonic and IR ToF sensors for each setting of the IR sensor with noise calculated as the standard deviation of the 500 measurements. A target entirely filled the field-of-view of both sensors—at a sensor distance of $4\,\mathrm{m}$ the full diagonal angle-of-view of the target was $46.7°$. These measurements were captured in standard fluorescent laboratory lighting, measured at $667\,\mathrm{lux}$ (see a discussion in Section III-B on quantifying ambient lighting for IR ToF sensors). The middle panel of Fig. 2 shows the percent error for both sensors. No corrections for temperature or humidity were applied to the ultrasonic sensor measurements, so the data were corrected for scale error using a best fit line to the linear portion. On the other hand, calibration was not needed for the IR ToF sensor. For a 73% reflective target the IR sensor shows an error magnitude less than 2% for distances up to $3000\,\mathrm{mm}$. The IR sensor noise displays three distinct regimes with target distance. At an in-close target distance of less than $200\,\mathrm{mm}$ the noise increases as the sensor moves closer to the target since fewer SPADs are enabled. In a middle regime ($\approx 200 - 800\,\mathrm{mm}$) the noise is nearly constant with target distance and reaches a minimum standard deviation of $1.5\,\mathrm{mm}$. At long target distances, the noise increases quadratically with target distance since the received signal falls by the square of the distance. The transitions between these regimes depend on target reflectivity. The ultrasonic measurements show a noise that exceeds $5\,\mathrm{mm}$ for all distances at or exceeding $500\,\mathrm{mm}$ and a non-linearity exceeding 2% for target distances of $800\,\mathrm{mm}$ or greater.

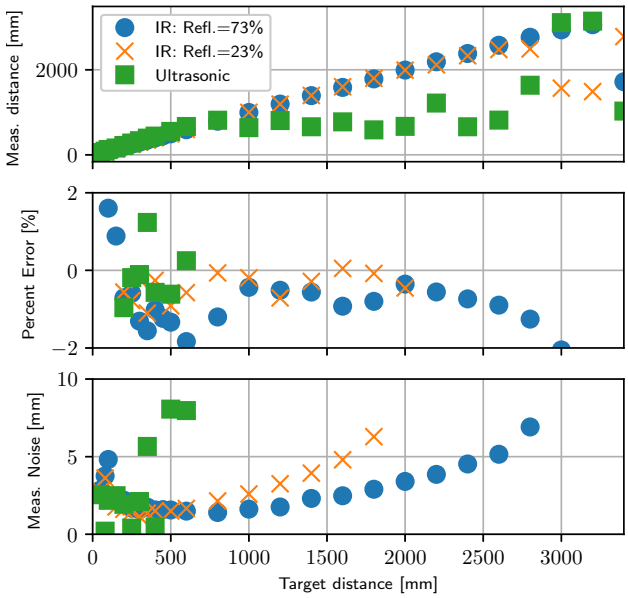

Fig. 2. The measured distance, percent error, and noise evaluated for the IR ToF and the ultrasonic ranging device. The fixed target is rigid foam core, $2.44\,\mathrm{m} \times 2.44\,\mathrm{m}$, painted for the target reflectivity. The IR sensor is configured for medium ranging with a timing budget of $33\,\mathrm{ms}$. At each target distance the actual distance is that measured with the 414D laser distance meter.

The VL53L1X ToF sensor measures signal and ambient rates, in addition to target distance. Recognizing that the dominant noise source in the IR ToF sensor is interfering ambient light, Fig. 3 demonstrates the relationships between signal rate, ambient rate, and noise. Fig. 3 panels (a,b) show the signal and ambient rate per SPAD, respectively, versus the target distance. The ambient rate depends on the target reflectivity since much of the ambient light received by the sensor first reflects off of the target. Panel (c) shows that the signal rate alone does not predict the measured noise, whereas Fig. 3 panel (d) demonstrates that the noise depends on the ratio of the signal rate to the ambient rate (or SBR for signal-to-background ratio) is a predictor of the noise. As the SBR reaches and falls beneath 10 the distance measurement noise begins to sharply increase, while at a ratio of 4 the measurement is unusable.

Given a signal rate and ambient rate at one target position, system design benefits from a prediction of performance at a modified distance. Fig. 4 demonstrates experimental verification of the expected signal falloff of $1/r^2$ for both target reflectivities for a target that covers the entire sensor FOV.

Copyright (c) 2020 IEEE. Personal use is permitted. For any other purposes, permission must be obtained from the IEEE by emailing pubs-permissions@ieee.org.

This is the author's version of an article that has been published in this journal. Changes were made to this version by the publisher prior to publication.
The final version of record is available at http://dx.doi.org/10.1109/JSEN.2020.2971595

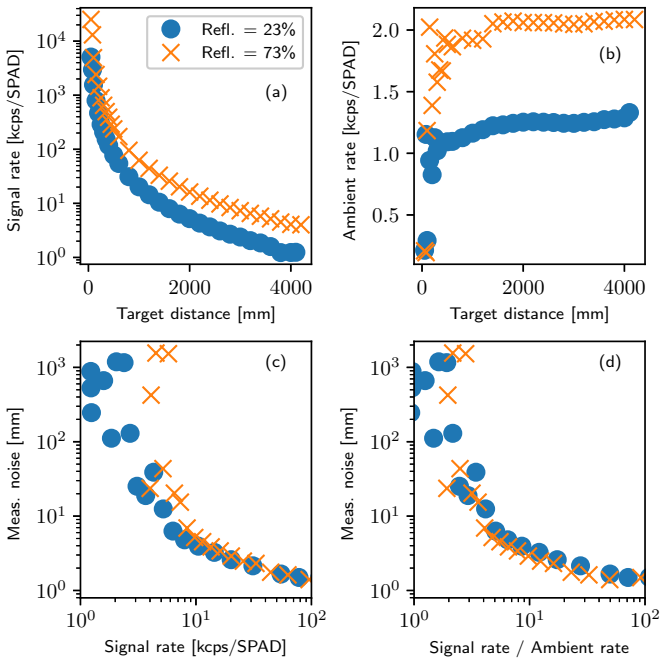

Fig. 3. Signal and ambient count rates per enabled SPAD for the IR ToF sensor for two different target reflectivities (Refl.). The sensor was configured for 'medium' ranging mode and a timing budget of 33 ms.

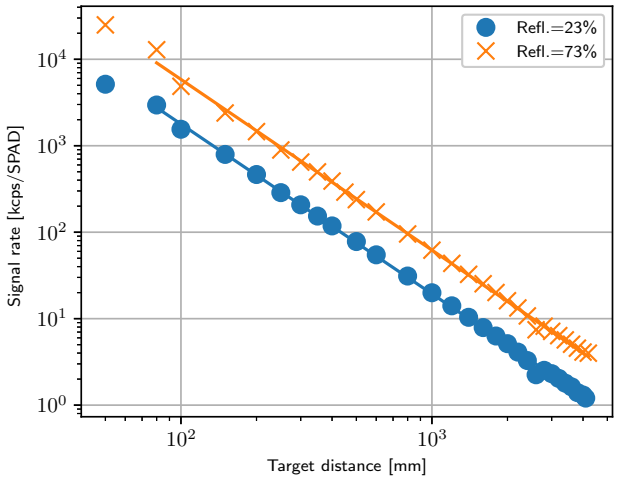

Fig. 4. The signal rate versus target distance. Lines are linear fits to the log transformed data for target ranges greater than 60 mm. The fits return slopes of -1.97 and -1.96, for reflectivities of 73% and 23%, respectively, demonstrating the anticipated $1/r^2$ signal falloff.

B. Performance versus ambient intensity

Fig. 5 shows the ranging noise of the ToF sensor as the ambient illumination is varied. An IR light-emitting diode (LED, LST1-01F09-IR04-00), with a center wavelength of 940 nm and full-width at half-maximum of 80 nm, was placed behind the ToF sensor and oriented to completely illuminate the target (73% reflectivity). This configuration ensured that the ambient illumination uniformly covered the FOV of the ToF sensor since light was first reflected by the target. From datasheet specifications of the IR LED, the maximum optical flux tested was 1070 mW into a cone with half-angle of 45°. At the two tested distances of 1000 mm and 1700 mm the calculated maximum irradiances onto the target were 580 $\mathrm{mW/m^2}$ and 200 $\mathrm{mW/m^2}$ respectively (by comparison, direct normal solar irradiance from 890-990 nm is 56.7 $\mathrm{W/m^2}$ [31]). Fig. 5 shows the depth measurement noise as the current through the LED is adjusted to change the ambient count rate. The ambient signal rate is the dominant source of noise and grows roughly linearly from a baseline noise level. As shown in Figs. 2 and 3, the sensor performance beyond a noise of 10 mm degrades considerably with inaccuracy exceeding ±2%, so we define the threshold of tolerable interfering irradiance at a noise of 10 mm. Extrapolating the noise measurements of Fig. 5 to 10 mm determines a tolerable irradiance on the target of 1250 $\mathrm{mW/m^2}$ and 275 $\mathrm{mW/m^2}$ at target distances of 1000 m and 1700 m, respectively, for irradiance centered at 940 nm.

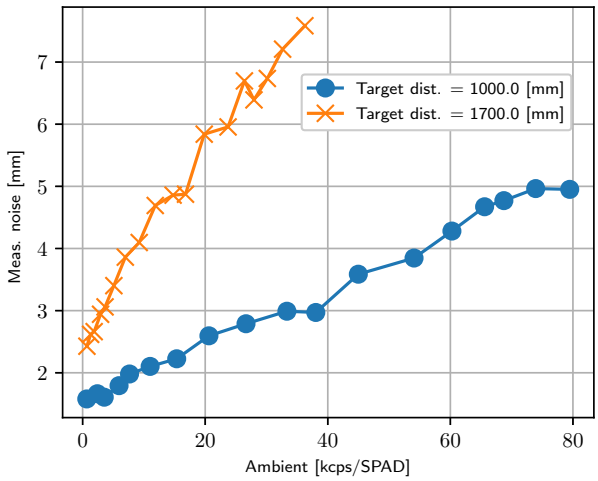

Fig. 5. ToF measurement noise versus the ambient count rate for a 33 ms timing budget and medium ranging setting. Controlled interfering ambient illumination was generated using an IR LED with a 940 nm center wavelength. The point of highest ambient intensity corresponds to 580 $\mathrm{mW/m^2}$ on the target. The average signal rate was 60.8 kcps/SPAD for the 1.0 m distance and 22.0 kcps/SPAD for the 1.7 m distance.

Ambient illumination must be carefully reported for optical ToF measurements. ToF receivers include an optical bandpass filter, typically of a spectral width of 50-100 nm, that transmits photons at the wavelength of the emitter while attenuating out-of-band photons [7]. The VL53L1X, for example, has an optical bandpass filter centered near 940 nm, the wavelength of the laser. Illuminance (SI unit of lux) is an incomplete measure of the ambient illumination intensity in the wavelength relevant to a ToF sensor; if lux is reported the spectrum of the ambient illumination must also be included to determine the number of interfering photons within the bandpass of the ToF filter [7]. Consider a few examples assuming a 890-990 nm ToF sensor bandpass. For black bodies at 638 lux and temperatures of 5778 K (solar) and 2810 K (incandescent) we calculate photon counts of 2.1×10^{18} $\mathrm{m^{-2}}$ and 1.3×10^{19} $\mathrm{m^{-2}}$, respectively from 890-990 nm. Finally, for our fluorescent laboratory lights using measured spectra we expect only 2.3×10^{17} $\mathrm{m^{-2}}$

Copyright (c) 2020 IEEE. Personal use is permitted. For any other purposes, permission must be obtained from the IEEE by emailing pubs-permissions@ieee.org.

This is the author's version of an article that has been published in this journal. Changes were made to this version by the publisher prior to publication.
The final version of record is available at http://dx.doi.org/10.1109/JSEN.2020.2971595

photons from 890-990 nm at an illuminance of 638 lux. The passband of a ToF sensor may differ from this example, however, the important conclusion that the photon counts in the passband can vary by over $\times 50$ at constant illuminance but with a different spectrum holds.

C. Programmable region of interest

The VL53L1X sensor supports a configurable region-of-interest (ROI) feature. A subset of the 16×16 SPAD array can be enabled to limit and point the viewing angle of the depth sensor. The datasheet specifies diagonal FOVs of 27°, 20°, and 15°, for enabled array sizes of 16×16, 8×8, and 4×4, respectively. Here, we characterize the angular resolution, and angular pointing of the ROI capability and describe the result when two targets of different depths are present in the field-of-view. Finally, we discuss how a dynamic ROI supports the generation of depth maps.

To characterize the angular pointing of the ROI, the depth of a flat background target was measured while stepping the position of a 4×4 enabled SPAD region through the 16×16 full array. As the measurement angle increases the returned photons travel a longer distance, and thus a greater depth is reported by the sensor. Given the flat background, the half-angle ($\theta/2$) relates to the measured depth (d) and the normal distance to the target (x) by: $\theta/2 = \arccos(x/d)$.

Fig. 6 shows the average angle measured versus 4×4 ROI position within the 16×16 array. An average single-pixel step

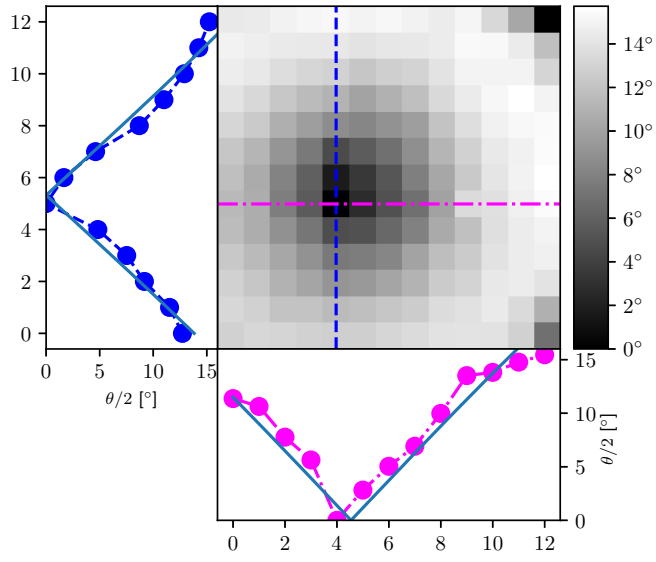

Fig. 6. The central grayscale image shows the average pointing angle ($\theta/2$) measured for all positions of a 4×4 ROI within the 16×16 sensor array. The left and bottom sub-panels show the response at a single column across rows (left, blue) and the response at a single row across columns (bottom, magenta). The locations of the line profiles are indicated by dashed lines applied on the image. The light blue lines are fits to $\theta/2 = \arctan((x - x_0)/f)$.

of the ROI moves the pointing by 2.5°. The maximum off-axis pointing measured is 15.7°. Note that, as shown in Fig. 6, the optical center of the lens system may deviate from the nominal center of the array by a few pixels and certain corner ROI locations return incorrect values due to occluded and disabled pixels. These measurements demonstrate the programmable pointing of the VL53L1X, which extends the functionality beyond that of a fixed FOV sensor by allowing an algorithm to locate the position of a hazard or search for a direction free of hazards. The line cuts in Fig. 6 display a fit to the expected dependence of the angular pointing upon the ROI position on the array: $\theta/2 = \arctan((x - x_0)/f)$ where x is the ROI position index and x_0 and f are fitting parameters. Near the array middle the angular pointing shifts more rapidly versus ROI position than predicted by a camera lens model, while at the array periphery the pointing shifts less rapidly. We expect that spatial nonuniformity of the emitter intensity causes this result.

To characterize the sensor angular resolution a target was suspended in the center of the field-of-view near the sensor, while a background that filled the entire sensor field-of-view was placed behind the near target. Fig. 8 shows depth measurements of a near target which fills 15.5° of the sensor FOV. This target is too large to inconclusively isolate and locate. On the other hand, Fig. 7 displays depth measurements of a target placed 1000 mm from the sensor; this target, which covers a diagonal FOV of 10.9°, is isolated from the background. As seen in Fig. 7 the depth measurement transitions from near to far in two ROI steps, confirming a spatial resolution of ~5°.

The sensor configurations of timing budget and ranging mode impact the spatial resolution and ability to discriminate between two depths. Fig. 9 demonstrates that a sufficient timing budget is required to isolate the near and far target. At a timing budget of 20 ms the returned depth, inside and outside of the near target, is a mixture of the depth of the near and far target. The longer timing budget of 33 ms allows for complete discrimination of the two depths.

Can this sensor detect the presence of a photon black hole? Consider a target of low reflectivity, R_2, in the center of the field-of-view and a distance x in front of a background of high reflectivity, R_1, which fills the entire field-of-view. Fig. 10 displays the signal rate and the measured distance versus the distance between the sensor and the background target for two ROI configurations and three target scenarios:

1) An 8% reflective near target of size 0.13 m × 0.13 m centered on a large background target of 73% reflectivity ($R_2 = 0.08$, $R_1 = 0.73$, $x = 0$ m, ×).
2) The same 8% reflective target positioned 1 m in front of the large 73% reflective background target ($R_2 = 0.08$, $R_1 = 0.73$, $x = 1$ m, +).
3) The large 73% reflectivity background target only ($R_2 = 0$, $R_1 = 0.73$, •).

As seen in Fig. 10 (c) the depth measurement from a 16×16 ROI does not indicate the presence of the near target until the sensor is 500 mm from the near target. However, as shown in (d) a constrained ROI of 4×4 detects the near target at further distances. The accuracy of the near target measured distance improves as the sensor is closer to the target. The presence of two targets at different distances is apparent from the non-

Copyright (c) 2020 IEEE. Personal use is permitted. For any other purposes, permission must be obtained from the IEEE by emailing pubs-permissions@ieee.org.

This is the author's version of an article that has been published in this journal. Changes were made to this version by the publisher prior to publication.
The final version of record is available at http://dx.doi.org/10.1109/JSEN.2020.2971595

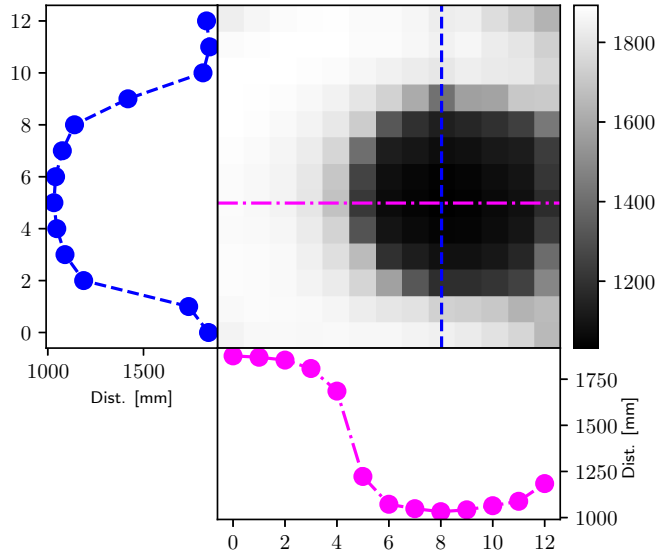

Fig. 7. An image map with false color representing the measured depth from an ROI scan with a 33 ms timing budget and short ranging. A rectangular target (135 ×130 mm) with reflectivity of 73% was placed a distance of 1000 mm to fill a diagonal FOV of 10.9°. A background with reflectivity of 23% was 1700 mm from the sensor and filled the entire sensor field of view. The left and bottom sub-panels show the response at a single column across rows (left, blue) and the response at a single row across columns (bottom, magenta). The locations of the line profiles are indicated by dashed lines applied on the image.

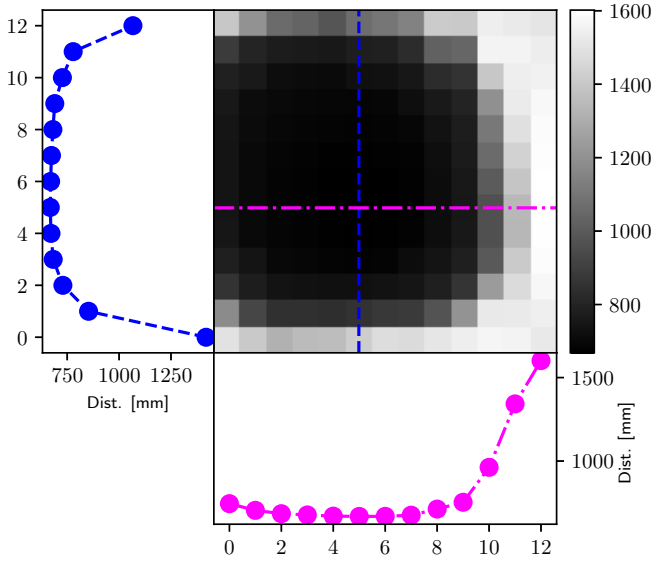

Fig. 8. An image map with false color representing the measured depth from an ROI scan with a 33 ms timing budget and short ranging. A rectangular target (135 ×130 mm) with reflectivity of 73% was placed a distance of 700 mm to fill a diagonal FOV of 15.5°. A background with reflectivity of 23% was 1700 mm from the sensor and filled the entire sensor field of view. The left and bottom sub-panels show the response at a single column across rows (left, blue) and the response at a single row across columns (bottom, magenta). The locations of the line profiles are indicated by dashed lines applied on the image.

linearity of the measured distance versus actual distance for scenario 2. With the sensor closer, the angular size of the smaller near target is larger such that the weighted returned distance favors the near target.

Fig. 10 panels (c) and (d) show that the measured distance is not sufficient to detect targets of two reflectivities at the same depth. However, the measured signal rate provides insight. The signal rate, SR, with the sensor a distance r from the background is proportional to:

$$SR(r) \propto \frac{R_1}{r^2}\left[1 - \frac{C_1}{(r-x)^2}\right] + \frac{R_2}{(r-x)^2}\left[\frac{C_1}{(r-x)^2}\right]. \quad (1)$$

The two terms in square brackets represent the area fraction of the background target and the near target, respectively, with C_1 a constant. As shown in Fig. 10 (b) the signal rate trends differently versus distance for scenario 1 than scenario 3. The near plateau of signal rate of scenario 1 in panel (b) around a distance of 1000 mm indicates that the solid angle covered by a low reflectivity target increases with the sensor closer to the targets. Fits to the form of the signal rate (SR) given by Equation 1 are shown as dashed lines and indicate the validity of the model.

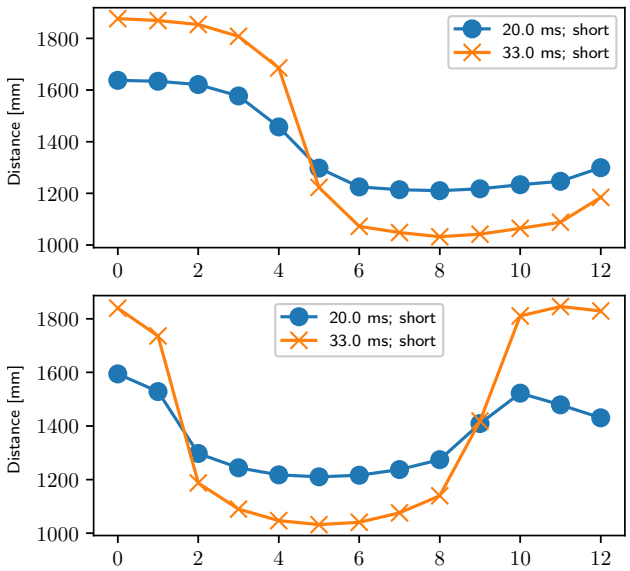

Fig. 9. ROI image line profiles for two sensor configuration. The target reflectivity is 73% and the background reflectivity is 23%.

Copyright (c) 2020 IEEE. Personal use is permitted. For any other purposes, permission must be obtained from the IEEE by emailing pubs-permissions@ieee.org.

This is the author's version of an article that has been published in this journal. Changes were made to this version by the publisher prior to publication.
The final version of record is available at http://dx.doi.org/10.1109/JSEN.2020.2971595

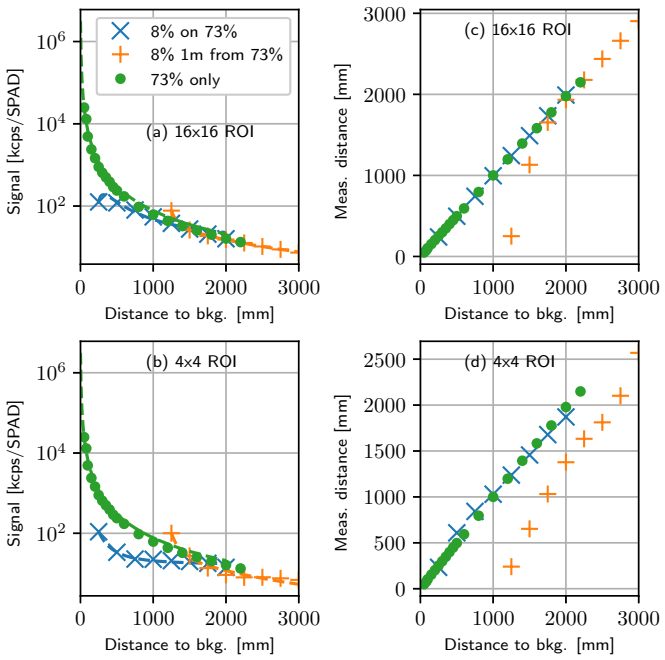

Fig. 10. (a) The signal rate for the full, 16×16 ROI. (b) The signal rate for a 4×4 ROI centered on the near target. The measured depth for a 16×16 ROI (c) and a 4×4 ROI (d).

IV. Inertial Measurement Unit for Sensor Pointing

The pointing of a depth sensor used for hazard detection may not be held constant by the user. Furthermore, natural or intentional pointing variations combined with measurements of the sensor pointing allows the system to search for an object or a direction that is free of hazards. We discuss and evaluate an inertial measurement unit (IMU) that fuses data from a 3-axis accelerometer, gyroscope, and magnetometer to provide the Euler angles necessary to correlate each depth measurement with ToF sensor pointing. The Bosch BNO055 is a "9-axis" absolute orientation sensor that processes the data from the sensors on-chip to provide orientation information as Euler angles and Quaternions, as well as linear acceleration. The output orientation angles have a resolution of $0.0625°$. In 9 degree-of-freedom mode, which enables absolute orientation outputs, the supply current is $12.5\,\mathrm{mA}$ at a supply of $3\,\mathrm{V}$ for a power consumption of $37.5\,\mathrm{mW}$.

We exercised the BNO055 to understand how the readout rate and the orientation measurements correspond with the timing budget and angular resolution of the IR ToF sensor. The absolute orientation fusion data was read at a rate of $100\,\mathrm{Hz}$, which provides an average of 3.3 orientation measurements for each $33\,\mathrm{ms}$ timing window of the IR ToF sensor. In $10\,\mathrm{ms}$ we read 26 consecutive I2C registers for three orientation angles, Quaternions, three axes of linear acceleration, and three axes of the gravity vector. Investigation of the orientation angle data shows that the noise of the orientation data is less than $0.01°$ on each of heading, pitch, and roll (when the sensor is still for $1.5\,\mathrm{s}$ following aggressive motion). This measured noise performance of the orientation measurements is considerably less than the resolution of the angular pointing of the IR ToF sensor, such that orientation measurement noise will not limit system resolution. Dynamic measurements of aggressive hand-motion show an RMS motion of $2.8°$ in a $30\,\mathrm{ms}$ window, which contributes an equivalent of around one ROI step of blur. System processing will use the IMU data to map the sensor orientation to each depth measurement and to reject a subset of depth measurements captured during periods of significant sensor motion ($\sim 5°$ or greater in $30\,\mathrm{ms}$) that blur the spatial resolution of the depth measurement. Furthermore, the timing budget of the IR ToF sensor may be dynamically adjusted based on the instantaneous rate of variation of the sensor orientation.

V. Conclusions and Future Work

We have presented characterization methods and results of the VL53L1X infrared ToF depth sensor that demonstrates range, distance noise, and nonlinearity. These characterization methods are generally applicable to ToF depth sensors. Measurement noise is dominated by ambient illumination and is found to degrade significantly when the ratio of signal count rate to ambient count rate falls below ~ 4. This ratio is impacted by the target reflectivity, target distance (falloff by $1/r^2$), and the intensity of the ambient illumination. The VL53L1X incorporates a programmable ROI which allows shifts of the sensor pointing off-axis by up to $15.7°$ in steps of $2.5°$, thus enabling spatial resolution in a miniaturized ToF sensor. Finally, a companion IMU was identified and evaluated that provides sensor pointing at a $100\,\mathrm{Hz}$ rate. The IMU resolution and noise performance were measured and found to not limit the angular resolution of the system. Future work will couple the IMU and ToF sensor to dynamically construct hazard maps using the system pointing as measured by the IMU and the ROI position of the ToF sensor. Microcontroller algorithms will be developed that respond to scenarios. For example, the system could search for and locate hazards, detect hazard-free directions, or move the ROI to avoid a region of significant ambient illumination.

Acknowledgment

L. Koerner acknowledges laboratory start-up funding from the University of St. Thomas School of Engineering. R. Jans acknowledges support from the University of St. Thomas Undergraduate Research Opportunities Program.

References

[1] P. Veelaert and W. Bogaerts, "Ultrasonic potential field sensor for obstacle avoidance," *IEEE Transactions on Robotics and Automation*, vol. 15, no. 4, pp. 774–779, 1999. [Online]. Available: http://dx.doi.org/10.1109/70.782033

[2] N. S. Ahmad, N. L. Boon, and P. Goh, "Multi-sensor obstacle detection system via model-based state-feedback control in smart cane design for the visually challenged," *IEEE Access*, vol. 6, pp. 64 182–64 192, 2018. [Online]. Available: http://dx.doi.org/10.1109/ACCESS.2018.2878423

[3] A. S. Al-Fahoum, H. B. Al-Hmoud, and A. A. Al-Fraihat, "A smart infrared microcontroller-based blind guidance system," *Active and Passive Electronic Components*, vol. 2013, pp. 1–7, 2013. [Online]. Available: http://dx.doi.org/10.1155/2013/726480

[4] J. Majchrzak, M. Michalski, and G. Wiczynski, "Distance estimation with a long-range ultrasonic sensor system," *IEEE Sensors Journal*, vol. 9, no. 7, pp. 767–773, Jul 2009. [Online]. Available: http://dx.doi.org/10.1109/JSEN.2009.2021787

Copyright (c) 2020 IEEE. Personal use is permitted. For any other purposes, permission must be obtained from the IEEE by emailing pubs-permissions@ieee.org.

This is the author's version of an article that has been published in this journal. Changes were made to this version by the publisher prior to publication.
The final version of record is available at http://dx.doi.org/10.1109/JSEN.2020.2971595

[5] B. Barshan, "Fast processing techniques for accurate ultrasonic range measurements," *Measurement Science and Technology*, vol. 11, no. 1, pp. 45–50, Dec 1999. [Online]. Available: http://dx.doi.org/10.1088/0957-0233/11/1/307

[6] R. Madli, S. Hebbar, P. Pattar, and V. Golla, "Automatic detection and notification of potholes and humps on roads to aid drivers," *IEEE Sensors Journal*, vol. 15, no. 8, pp. 4313–4318, Aug 2015. [Online]. Available: http://dx.doi.org/10.1109/JSEN.2015.2417579

[7] A. Süss, V. Rochus, M. Rosmeulen, and X. Rottenberg, "Benchmarking time-of-flight based depth measurement techniques," *Smart Photonic and Optoelectronic Integrated Circuits XVIII*, Mar 2016. [Online]. Available: http://dx.doi.org/10.1117/12.2212478

[8] B. Hosticka, P. Seitz, and A. Simoni, "Optical time-of-flight sensors for solid-state 3d-vision," *Encyclopedia of sensors*, vol. 7, pp. 259–289, 2006.

[9] T. Okoshi, *Three-dimensional imaging techniques*. Elsevier, 2012.

[10] N. A. W. Dutton, T. Al Abbas, F. M. D. Rocca, N. Finlayson, B. Rae, and R. K. Henderson, "Time of flight imaging and sensing for mobile applications," *Low-Power Analog Techniques, Sensors for Mobile Devices, and Energy Efficient Amplifiers*, pp. 221–249, 2019. [Online]. Available: http://dx.doi.org/10.1007/978-3-319-97870-3_12

[11] W. Elmannai and K. Elleithy, "Sensor-based assistive devices for visually-impaired people: Current status, challenges, and future directions," *Sensors*, vol. 17, no. 3, p. 565, Mar 2017. [Online]. Available: http://dx.doi.org/10.3390/s17030565

[12] D. Inc. Duracell DX1500 rechargable AA. [Online]. Available: https://www.duracell.com/en-us/techlibrary/product-technical-data-sheets

[13] D. Van Nieuwenhove, W. van der Tempel, R. Grootjans, J. Stiens, and M. Kuijk, "Photonic demodulator with sensitivity control," *IEEE Sensors Journal*, vol. 7, no. 3, pp. 317–318, Mar 2007. [Online]. Available: http://dx.doi.org/10.1109/JSEN.2006.890164

[14] T. Oggier, R. Kaufmann, M. Lehmann, B. Buttgen, S. Neukom, M. Richter, M. Schweizer, P. Metzler, F. Lustenberger, and N. Blanc, "Novel pixel architecture with inherent background suppression for 3d time-of-flight imaging," *Videometrics VIII*, Jan 2005. [Online]. Available: http://dx.doi.org/10.1117/12.586933

[15] D. Stoppa, L. Pancheri, N. Massari, M. Malfatti, M. Perenzoni, G. Pedretti, and G. F. Dalla Betta, "Time of flight image sensors in 0.18 μcmos technology: a comparative overview of different approaches," in *Proceedings of the international image sensor workshop*, 2011.

[16] L. V. Labs, "Helios embedded." [Online]. Available: https://dce9ugryut4ao.cloudfront.net/LUCID-Helios-Embedded-datasheet.pdf

[17] Infineon, "Product Brief: REAL3^{TM} image sensor family." [Online]. Available: https://www.infineon.com/dgdl/Infineon-REAL3+Image+Sensor+Family-PB-v01_00-EN.PDF?fileId=5546d462518ffd850151a0afc2302a58

[18] pmd and infineon, "Development kit brief: Camboard pico flexx." [Online]. Available: https://pmdtec.com/picofamily/wp-content/uploads/2018/03/PMD_DevKit_Brief_CB_pico_flexx_CE_V0218-1.pdf

[19] E. Charbon and M. W. Fishburn, "Monolithic single-photon avalanche diodes: SPADs," *Single-Photon Imaging*, pp. 123–157, 2011. [Online]. Available: http://dx.doi.org/10.1007/978-3-642-18443-7_7

[20] D. Bronzi, F. Villa, S. Tisa, A. Tosi, and F. Zappa, "SPAD figures of merit for photon-counting, photon-timing, and imaging applications: A review," *IEEE Sensors Journal*, vol. 16, no. 1, pp. 3–12, Jan 2016. [Online]. Available: http://dx.doi.org/10.1109/JSEN.2015.2483565

[21] N. Dutton, J. Vergote, S. Gnecchi, L. Grant, D. Lee, S. Pellegrini, B. Rae, and R. Henderson, "Multiple-event direct to histogram tdc in 65nm fpga technology," *2014 10th Conference on Ph.D. Research in Microelectronics and Electronics (PRIME)*, Jun 2014. [Online]. Available: http://dx.doi.org/10.1109/PRIME.2014.6872727

[22] N. A. W. Dutton, S. Gnecchi, L. Parmesan, A. J. Holmes, B. Rae, L. A. Grant, and R. K. Henderson, "11.5 a time-correlated single-photon-counting sensor with 14gs/s histogramming time-to-digital converter," *2015 IEEE International Solid-State Circuits Conference - (ISSCC) Digest of Technical Papers*, Feb 2015. [Online]. Available: http://dx.doi.org/10.1109/ISSCC.2015.7062997

[23] T. Al Abbas, N. A. Dutton, O. Almer, N. Finlayson, F. M. D. Rocca, and R. Henderson, "A CMOS SPAD sensor with a multi-event folded flash time-to-digital converter for ultra-fast optical transient capture," *IEEE Sensors Journal*, vol. 18, no. 8, pp. 3163–3173, Apr 2018. [Online]. Available: http://dx.doi.org/10.1109/JSEN.2018.2803087

[24] *AFBR-S50MV85G Time-of-Flight Sensor Module for Distance and Motion Measurement: Data Sheet*, Afbr-s50mv85g-ds102 ed., Broadcom, Dec 2018.

[25] *VL53L0X Datasheet*, 2nd ed., ST, April 2018.

[26] N. Lakovic, M. Brkic, B. Batinic, J. Bajic, V. Rajs, and N. Kulundzic, "Application of low-cost vl53l0x tof sensor for robot environment detection," *2019 18th International Symposium INFOTEH-JAHORINA (INFOTEH)*, Mar 2019. [Online]. Available: http://dx.doi.org/10.1109/INFOTEH.2019.8717779

[27] *VL53L1X Datasheet*, 3rd ed., ST, Nov 2018.

[28] M. O. Khyam, S. S. Ge, X. Li, and M. R. Pickering, "Highly accurate time-of-flight measurement technique based on phase-correlation for ultrasonic ranging," *IEEE sensors journal*, vol. 17, no. 2, pp. 434–443, 2017.

[29] M. M. Saad, C. J. Bleakley, T. Ballal, and S. Dobson, "High-accuracy reference-free ultrasonic location estimation," *IEEE Transactions on Instrumentation and Measurement*, vol. 61, no. 6, pp. 1561–1570, Jun 2012. [Online]. Available: http://dx.doi.org/10.1109/TIM.2011.2181911

[30] R. M. Jans and L. J. Koerner. ToF depth sensor characterization data (VL53L1X). [Online]. Available: http://dx.doi.org/10.6084/m9.figshare.10070246

[31] "Standard tables for reference solar spectral irradiances: Direct normal and hemispherical on 37 ° tilted surface," ASTM International, Tech. Rep. ASTM G173-03(2012), 2012.

Copyright (c) 2020 IEEE. Personal use is permitted. For any other purposes, permission must be obtained from the IEEE by emailing pubs-permissions@ieee.org.